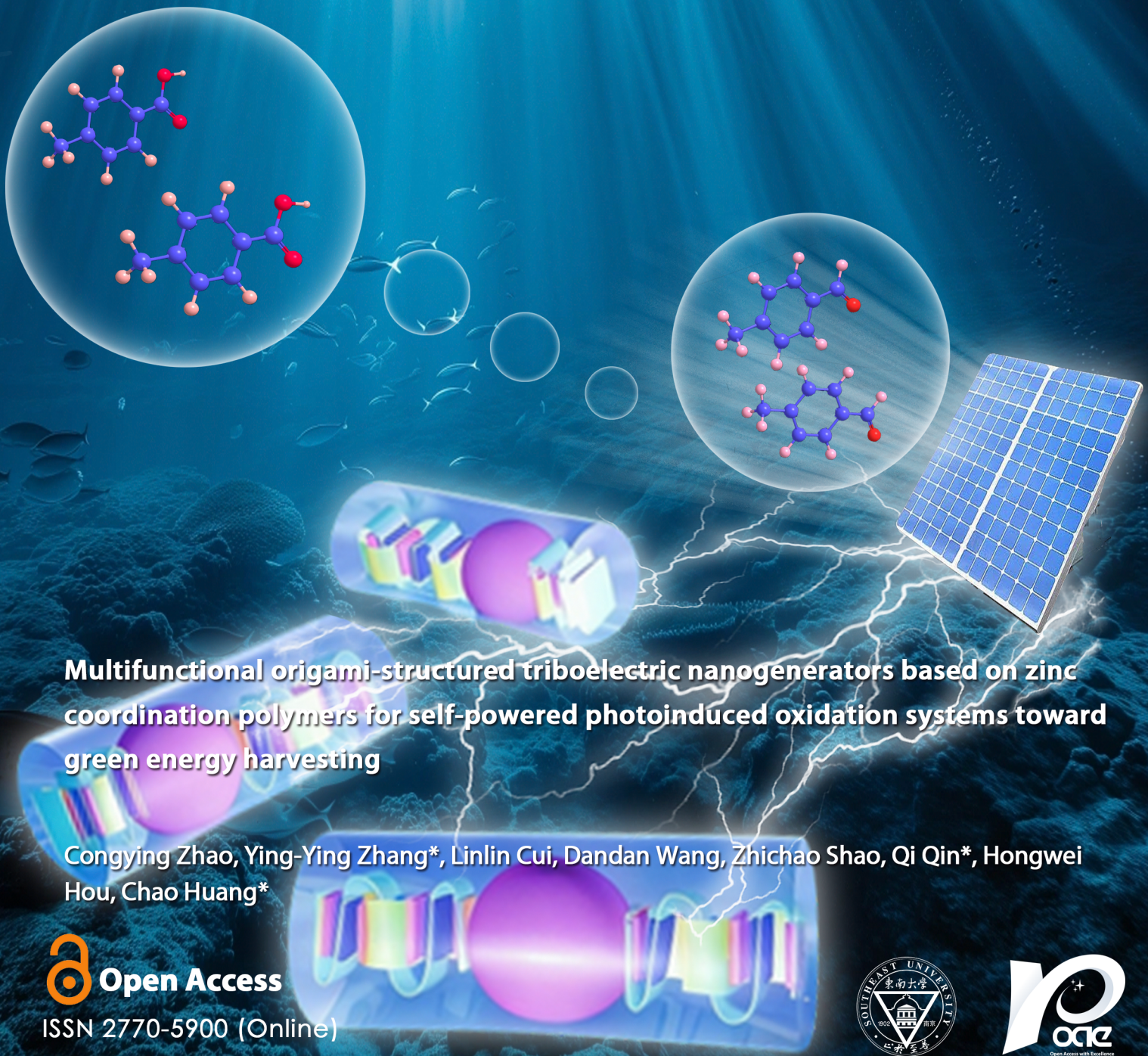
Volume 6, Issue 3, March 2026
DOI: 10.20517/energymater.2025.204

ENERGY MATERIALS

Editor-in-Chief: Prof. Yuping Wu



Multifunctional origami-structured triboelectric nanogenerators based on zinc coordination polymers for self-powered photoinduced oxidation systems toward green energy harvesting

Congying Zhao, Ying-Ying Zhang*, Linlin Cui, Dandan Wang, Zhichao Shao, Qi Qin*, Hongwei Hou, Chao Huang*

Open Access
ISSN 2770-5900 (Online)

Article | Open Access

Energy Materials

Zhao et al. Energy Mater. 2026, 6, 600023 DOI:10.20517/energymater.2025.204

Multifunctional origami-structured triboelectric nanogenerators based on zinc coordination polymers for self-powered photoinduced oxidation systems toward green energy harvesting

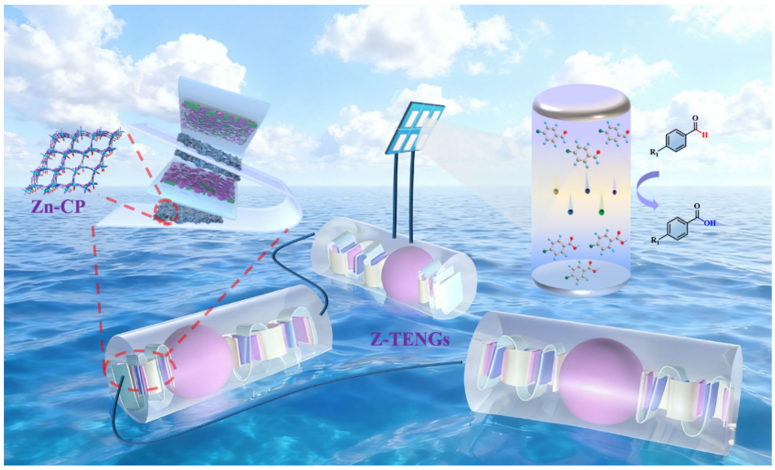
Congying Zhao[1], Ying-Ying Zhang[1,*], Linlin Cui[1], Dandan Wang[1], Zhichao Shao[1], Qi Qin[1,*], Hongwei Hou[2], Chao Huang[1,*]

Keywords:
Coordination polymers, composite film, multifunctional origami-structure, photoinduced system, triboelectric nanogenerators

Citation: Zhao, C.; Zhang, Y. Y.; Cui, L.; Wang, D.; Shao, Z.; Qin, Q.; Hou, H.; Huang, C. Multifunctional origami-structured triboelectric nanogenerators based on zinc coordination polymers for self-powered photoinduced oxidation systems toward green energy harvesting. *Energy Mater.* **2026**, *6*, 600023. https://dx.doi.org/10.20517/energymater.2025.204

Received: 24 Nov 2025 **First Decision:** 8 Dec 2025 **Revised:** 23 Dec 2025 **Accepted:** 20 Jan 2026 **Published:** 16 Mar 2026

Academic Editors: Sining Yun, Ho Seok Park **Copy Editor:** Fangling Lan **Production Editor:** Fangling Lan



Abstract

Development of multifunctional triboelectric nanogenerators (TENGs) capable of efficiently harvesting diverse low-frequency mechanical energies for self-powered systems remains a significant challenge. To address this issue, we designed and fabricated a zigzag-origami-structured TENG based on composite films by integrating a zinc coordination polymer (**Zn-CP**) with ethylcellulose (EC), aiming to convert human-motion and water-wave energies into electricity to drive a self-powered photo-induced oxidation system. A series of flexible **Zn-CP@EC** composite films with varying **Zn-CP** contents were prepared, among which the 10% **Zn-CP@EC** composite film exhibited the best triboelectric performance. By scaling the film dimensions and integrating multiple origami-structured 10% **Zn-CP@EC-TENGs** (**Z-TENGs**), the output performance was further enhanced, with the six-unit device (**Z-6**) showing the best performance under palm pressure. The **Z-6** device, encapsulated in a plastic enclosure, was deployed in an oscillating water tank to harvest wave energy, which successfully powered LEDs as light sources for the photo-induced oxidation of aldehydes to carboxylic acids with high selectivity and efficiency. This work demonstrates that CP-based composite films can serve as effective

[1]School of Materials Electronics and Energy Storage, and Center for Advanced Materials Research, Zhongyuan University of Technology, Zhengzhou 450007, Henan, China.
[2]College of Chemistry and Green Catalysis Center, Zhengzhou University, Zhengzhou 450001, Henan, China.

*Correspondence to: Dr. Ying-Ying Zhang, School of Materials Electronics and Energy Storage, and Center for Advanced Materials Research, Zhongyuan University of Technology, Zhengzhou 450007, Henan, China. E-mail: 6477@zut.edu.cn; Prof. Qi Qin, School of

Materials Electronics and Energy Storage, and Center for Advanced Materials Research, Zhongyuan University of Technology, Zhengzhou 450007, Henan, China. E-mail: qq@zut.edu.cn; Dr. Chao Huang, School of Materials Electronics and Energy Storage, and Center for Advanced Materials Research, Zhongyuan University of Technology, Zhengzhou 450007, Henan, China. E-mail: huangchao@zut.edu.cn

triboelectric materials for scalable TENGs, enabling the realization of self-powered photochemical systems driven by diverse environmental mechanical energies.

INTRODUCTION

With the continuous and rapid exploitation of fossil energy resources, energy-related challenges have become increasingly pronounced, leading to severe ecological environment degradation[1-4]. Consequently, the development of self-sustaining power generation systems that utilize renewable and clean energy sources has attracted growing attention and become an urgent societal and scientific demand[5-9]. As one of the most abundant and clean renewable energy sources on earth, mechanical energy offers significant potential for sustainable power generation, spurring the demand for advanced flexible and eco-friendly energy-harvesting devices[10-13]. Triboelectric nanogenerators (TENGs), based on electrostatic induction and contact electrification, have emerged as a promising technology for converting environmental mechanical energy into electricity, owing to their simple fabrication, readily available materials, and scalability[14-21]. Various strategies, including material selection and functionalization, and micro/nano- structural engineering, have been explored to enhance TENG output performance[22-26]. However, existing TENG devices still face a critical limitation: their insufficient efficiency in harvesting human motion and water-wave energy, which are characterized by low, random, and unpredictable frequencies[16,17,27-31]. This limitation underscores the critical need for targeted structural design and material optimization to improve TENG performance.

Hybrid organic-inorganic materials have been recognized as advanced triboelectric layers for TENGs, as they synergistically tune carrier diffusion lengths, band gap, and dielectric characteristics by combining organic and inorganic components[32-37]. Coordination polymers (CPs), as a class of hybrid organic-inorganic materials with highly ordered reticular structures, possess high structural designability, unique porous properties and high specific surface areas, providing robust platforms for triboelectric layers[38,39]. Their well-defined frameworks with precise distributions of metal nodes and organic ligands enable regulation of electron transport, polarity, and charge storage, thereby enhancing triboelectric performance[40-42]. However, the practical applications of CP-based triboelectric materials are hindered by their inherent deficiencies, such as poor stability, difficulty in large-scale preparation, and insufficient mechanical strength[38,41]. To address these issues, recent efforts have focused on developing CP-based self-supporting composites with excellent mechanical stability and outstanding processability[43,44]. In particular, integrating CPs with organic polymers has been proven effective in improving mechanical robustness and processability. However, most reported CP-based composite films are still fabricated into conventional planar TENG structures, which suffer from low space utilization and restricted contact area - key bottlenecks for efficient harvesting of low-frequency mechanical energy[45-56]. Thus, it is necessary to develop novel CP-based composite films with optimized structures for scalable low-frequency energy collection[57-59].

In this study, we designed a suitable and rationally designed zigzag-origami TENG that integrates numerous parts within a limited space and enables them to operate under different types of low-frequency mechanical energy. To achieve higher output performance and simulate practical applications in real-world conditions, **Zn-CP@EC** composite films were prepared by introducing a zinc coordination polymer (**Zn-CP**) into the organic polymer ethylcellulose (EC) at varying ratios, identifying the optimal **Zn-CP** content (10%) for peak triboelectric performance. These films were used to construct a scalable zigzag-origami structured 10% **Zn-CP@EC**-based TENG (**Z-TENGs**), capable of harvesting human movement and water-wave energy. To

further augment performance and demonstrate scalability, we constructed multi-unit integrated devices, denoted as **Z-2**, **Z-4**, and **Z-6**, corresponding to systems comprising two, four, and six 10% **Zn-CP@EC-TENG** units, respectively. Moreover, the **Z-6** device can be enclosed in a box to simulate water waves and harvest wave energy, converting it into electricity, which can continuously and sustainably drive the light-emitting diodes (LEDs) to provide illumination for executing self-powered photo-induced reactions without any energy devices. This self-powered system exhibited outstanding ability to promote the photo-induced oxidation of aldehydes to carboxylic acids.

EXPERIMENTAL

Materials. 4,5-di(2H-tetrazole-5-yl)-1H-imidazole-2-amino (NH_2-H_3idbt) was synthesized according to improved methods in the literature[60]. 2-Amino-4,5-dicyano-1H-imidazole (97%) was purchased from Shanghai Macklin Biochemical Co., Ltd (Shanghai, China). Triethylamine hydrochloride (99%) was bought from Shanghai Macklin Biochemical Co., Ltd (Shanghai, China). N, N-dimethylformamide (DMF) and Zinc sulfate heptahydrate ($ZnSO_4 \cdot 7H_2O$) were obtained from Shanghai Aladdin Biochemical Technology Co., Ltd. (Shanghai, China). P-Tolualdehyde (**2a**, 97%), Anisic aldehyde (**2b**, 98%), 4-Hydroxybenzaldehyde (**2c**, 97%), 4-(Methylthio) benzaldehyde (**2d**, 98%), 4-cyanobenzaldehyde (**2e**, 98%), and p-phenylbenzaldehyde (**2f**, 98%) were bought from Anhui Zesheng Technologies Co., Ltd. (Anhui, China). All reagents and solvents were commercially available without further purification.

Characterizations. The detailed characterization instruments, such as powder X-ray diffraction (PXRD), thermal gravimetric analyzer (TGA), and X-ray photoelectron spectroscopy (XPS) of **Zn-CP** and composite materials were given in the Supplementary Materials. Meanwhile, the Single-Crystal X-ray diffraction (SCXRD) test and crystal data were provided in the Supplementary Tables 1 and 2.

Synthesis of $\{[Zn(NH_2\text{-}H_3idbt)(H_2O)]\cdot H_2O\}_n$ (Zn-CP). NH_2-H_3idbt (22 mg, 0.1 mmol), $ZnSO_4 \cdot 7H_2O$ (28.7 mg, 0.1 mmol), DMF (3 mL) and H_2O (5 mL) were mixed in a 25 mL Teflon-lined stainless steel container for heating at 160 °C for 3 days, and white massive crystals of **Zn-CP** were obtained (yield, 65%, depended on Zn). Anal. Calcd (%) for $C_5H_8N_{11}O_2Zn$:C, 18.79%; H, 2.52%; N, 48.21%. Found: C, 18.81%; H, 2.53%; N, 48.24%. IR (KBr, cm^{-1}): 3462 (vw), 3323 (s), 3161 (m), 2928 (vw), 1543 (m), 1441 (m), 1382 (vw), 1256 (s), 1228 (vw), 1157 (m), 1123 (vw), 1037 (vw), 1021 (vw), 958 (s), 759 (s), 651 (vw), 628 (vw).

Assembly of Zn-CP@EC-TENGs. 3.75 g of polyvinylidene fluoride (PVDF), 8.5 g of DMF and 12.75 g of acetone were charged into a 50 mL round-bottom flask and stirred at 60 °C for 30 min. After cooling to room temperature, the mixed solution was spin-coated onto a Kapton film at 2,000 rpm for 90 s, then baked in an oven at 80 °C for 4 h to obtain the PVDF film. The back side of the Kapton film was subsequently attached to the adhesive side of a Cu tape, and a copper wire was bonded to the rear of the Cu tape with conductive silver epoxy to complete the negative electrode.

Dissolve powder EC (0.4 g) in DMF (6 mL) and magnetically stir at 100 °C for 30 min to obtain a homogeneous EC solution. In a separate centrifuge tube, disperse **Zn-CP** in 6 mL DMF at mass fractions of 1%, 5%, 10%, 15% and 20%, and sonicate the mixture for 30 min to ensure uniform dispersion. Combine the two solutions and continue stirring for 4 h to obtain a mixed solution. Cast the solution onto a clean glass plate and dry in an oven at 80 °C for 30 min to form a film. After peeling off the film, cut it into 5 cm × 5 cm squares and adhere each square to the adhesive side of a Cu tape. A copper wire was then bonded to the back of the copper tape with conductive silver epoxy, yielding **Zn-CP@EC** composite-film electrodes containing different mass fractions of **Zn-CP**. Spin-coated PVDF film and different-proportion **Zn-CP@EC** composite films were used as the negative and positive friction materials, respectively. They were combined to fabricate

Zn-CP@EC-TENG devices, working in the vertical contact-separation mode with an effective contact area of 5 × 5 cm^2.

Preparation of Z-2 device with different contact areas. Two PET films were cut into different size rectangles (1.5 × 5, 2.5 × 8, 3.5 × 11, 4.5 × 14, and 5.5 × 17 cm^2, respectively). Two positive electrodes (1 × 1, 2 × 2, 3 × 3, 4 × 4, and 5 × 5 cm^2, respectively) and two negative electrodes (1 × 1, 2 × 2, 3 × 3, 4 × 4, and 5 × 5 cm^2, respectively) were attached to the upper and lower sides of each PET rectangle, respectively. The two PET films were then positioned perpendicular to each other, bonded together, alternately folded, and finally sealed to complete the **Z-2** device.

Preparation of Z-2, Z-4, Z-6 measured at 5 × 5 cm^2. Two PET films were cut into different size rectangles (5.5 × 12, 5.5 × 22, and 5.5 × 32 cm^2, respectively). Two, four, or six 5 × 5 cm^2 positive electrodes and an equal number of 5 × 5 cm^2 negative electrodes were attached to the upper and lower sides of each of the two PET films, respectively. The two PET films were then positioned perpendicular to each other, bonded together, alternately folded, and finally sealed to complete the **Z-2**, **Z-4**, **Z-6** device.

RESULTS AND DISCUSSION

This study aims to design and fabricate a zigzag-origami-structured triboelectric nanogenerator [Figure 1A] based on **Zn-CP@EC** composite films for efficiently harvesting human-motion and water-wave energies to drive a self-powered photo-induced oxidation system. To that end, **Zn-CP** was synthesized by reacting NH_2-H_3idbt ligand and $ZnSO_4 \cdot 7H_2O$ to yield colorless single crystals, which served as photocatalyst and triboelectric material to explore their bifunctional properties. Single-crystal X-ray diffraction analysis (SCXRD) of **Zn-CP**, which has the space group *Pna2*$_1$, showed an orthorhombic net with a diamond-shaped framework containing hexanuclear Zn^{II} secondary building units (Zn-SBUs). The corresponding formula for **Zn-CP** was obtained by SCXRD, XPS, TGA, elemental analysis (EA), and charge-balance analyses [Supplementary Figure 1-3]. In **Zn-CP**, the asymmetric unit comprised one NH_2-$Hidbt^{2-}$ ligand, one Zn^{II} ion, and one coordinated H_2O molecule, respectively. The Zn^{II} ion had the characteristic octahedral geometry, ligated by one O atom from one coordinated H_2O molecule and five N atoms from three NH_2-$Hidbt^{2-}$ ligands [Supplementary Figure 4]. The fully deprotonated tetrazole groups had bridging and chelating coordination modes to connect with Zn^{II} ions, generating a hexanuclear Zn^{II} secondary building unit (Zn-SBUs) [Supplementary Figure 5]. Furthermore, these Zn-SBUs were interconnected by the coordination bonds of tetrazole-N atoms and Zn ions to form a diamond-shaped channel. These channels were bridged by tetrazole rings to construct a three-dimensional (3D) architecture [Figure 1B and C, Supplementary Figure 6].

To achieve precise molecular insights into the influence of the **Zn-CP**-based TENG output performance, the NH_2-H_3idbt ligand and **Zn-CP** were milled and assembled as positive-polarity triboelectrodes with negative-polarity polyvinylidene fluoride (PVDF) to fabricate **Zn-CP-TENG** and **NH_2-H_3idbt-TENG**, respectively. As shown in Supplementary Figure 7, the operation mode of the TENGs was regular contact-separation, where the flow of electrons was driven by the positive and negative triboelectric materials in the external circuit. The triboelectric output signals indicated that the **Zn-CP-TENG** demonstrated a much higher output performance, with short-circuit current (I_{sc}) and open-circuit voltage (V_{oc}) approximately two times higher than those of **NH_2-H_3idbt-TENG** [Supplementary Figure 8]. The higher outputs were mainly due to **Zn-CP** with a periodic and uniform arrangement of metal centers and ligands in the 3D network, which could improve the electron-donating capability to generate electrons significantly more easily and produce much more charge to enhance the **Zn-CP-TENG** outputs[61,62].

To enhance TENG output and improve the adaptability of CPs as triboelectric materials, organic polymers were integrated with CPs, the surface of the CPs was periodically modified, and well-proportioned composite

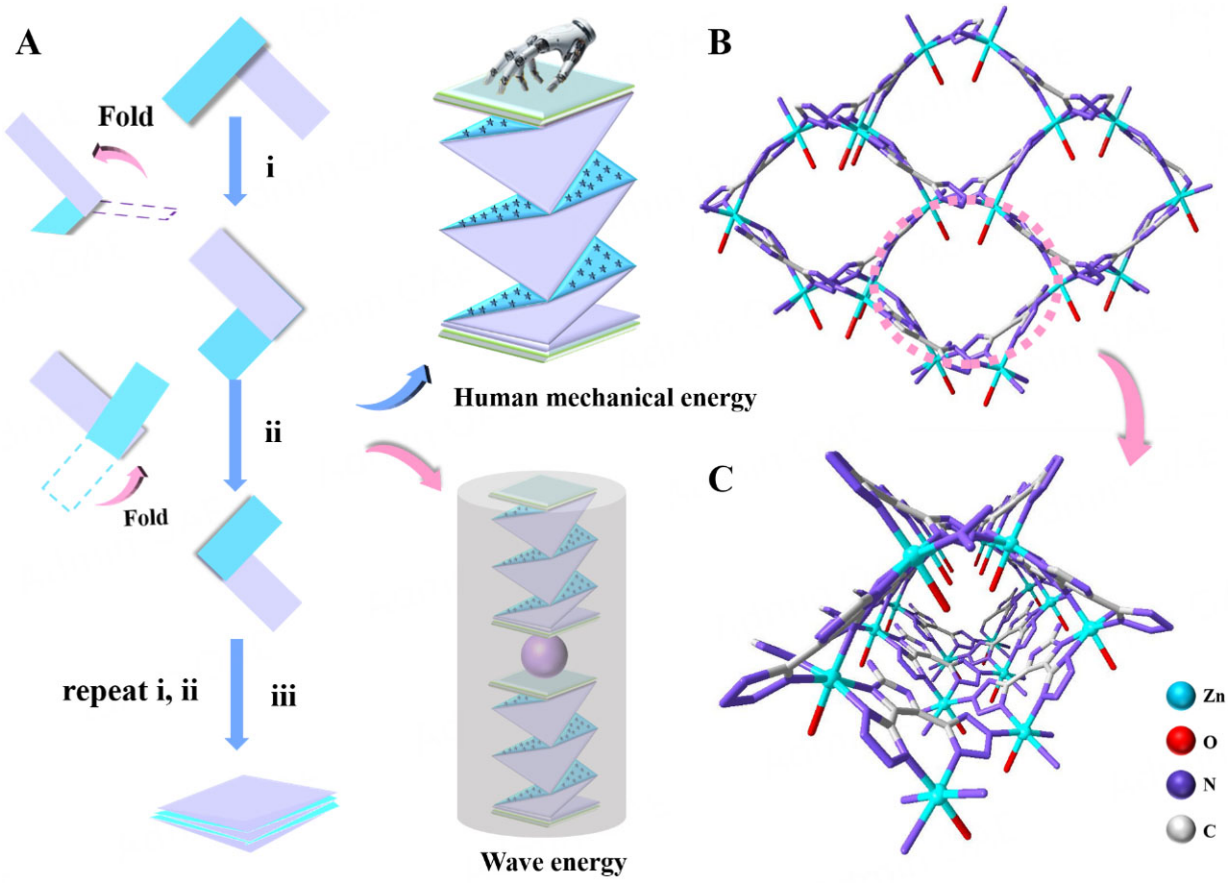


Figure 1. (A) Schematic illustration of CP-based TENG for the self-powered photoinduced applications. (B) A view of the 3D network of **Zn-CP**. (C) Perspective view of the open rhomboid channel.

films were fabricated. These films allow surface charge density (σ) to accumulate rapidly to a high initial value to provide a stable and high current in a brief period to increase the TENG outputs. Owing to its excellent electron-donating properties, film-forming capability, and flexibility, the organic polymer EC, which ranks just below Nylon-6 in the triboelectric series, was used to fabricate a series of **Zn-CP@EC** composite films [Figure 2A]. To assess the effect of **Zn-CP** on TENG output, **Zn-CP@EC** films with different **Zn-CP** contents (ranging from 1% to 20%) were prepared. These films were used as triboelectric layers to assemble **Zn-CP@EC-TENGs**. The scanning electron microscopy (SEM) images indicate that **Zn-CP** was firmly and uniformly loaded onto the EC to successfully induce **Zn-CP@EC** composite films [Supplementary Figure 9]. The corresponding cross-sectional SEM images demonstrated that the thicknesses of **Zn-CP@EC** composite films with different contents of **Zn-CP** (1%, 5%, 10%, 15%, and 20%, respectively) were similar to each other (25.3-26.9 μm), suggesting that the thicknesses of the **Zn-CP@EC** composite films had almost no effect on the outputs of the assembled **Zn-CP@EC-TENGs** [Supplementary Figure 10]. Meanwhile, surface roughness (Ra) measurements revealed that the **Zn-CP@EC** composite films with different **Zn-CP** ratios had similar Ra, indicating that the influence of Ra on the **Zn-CP@EC-TENGs** outputs could be ruled out [Supplementary Figure 11]. To further examine the impact of the **Zn-CP@EC-TENGs** output and the surface structure of the **Zn-CP@EC** composite films, we used Kelvin probe force microscopy (KPFM) surface potentials to evaluate the surface structure of the **Zn-CP@EC** composite films. As evident from Figure 2B and Supplementary Figure 12, the KPFM surface potentials of **Zn-CP@EC** composite films with different **Zn-CP** content changed significantly. Notably, when the content of **Zn-CP** in **Zn-CP@EC** composite films was 10%, the KPFM surface potential reached a maximum, which revealed that the 10% **Zn-CP@EC** composite film displayed the most positive potential to produce more electrons by integrating

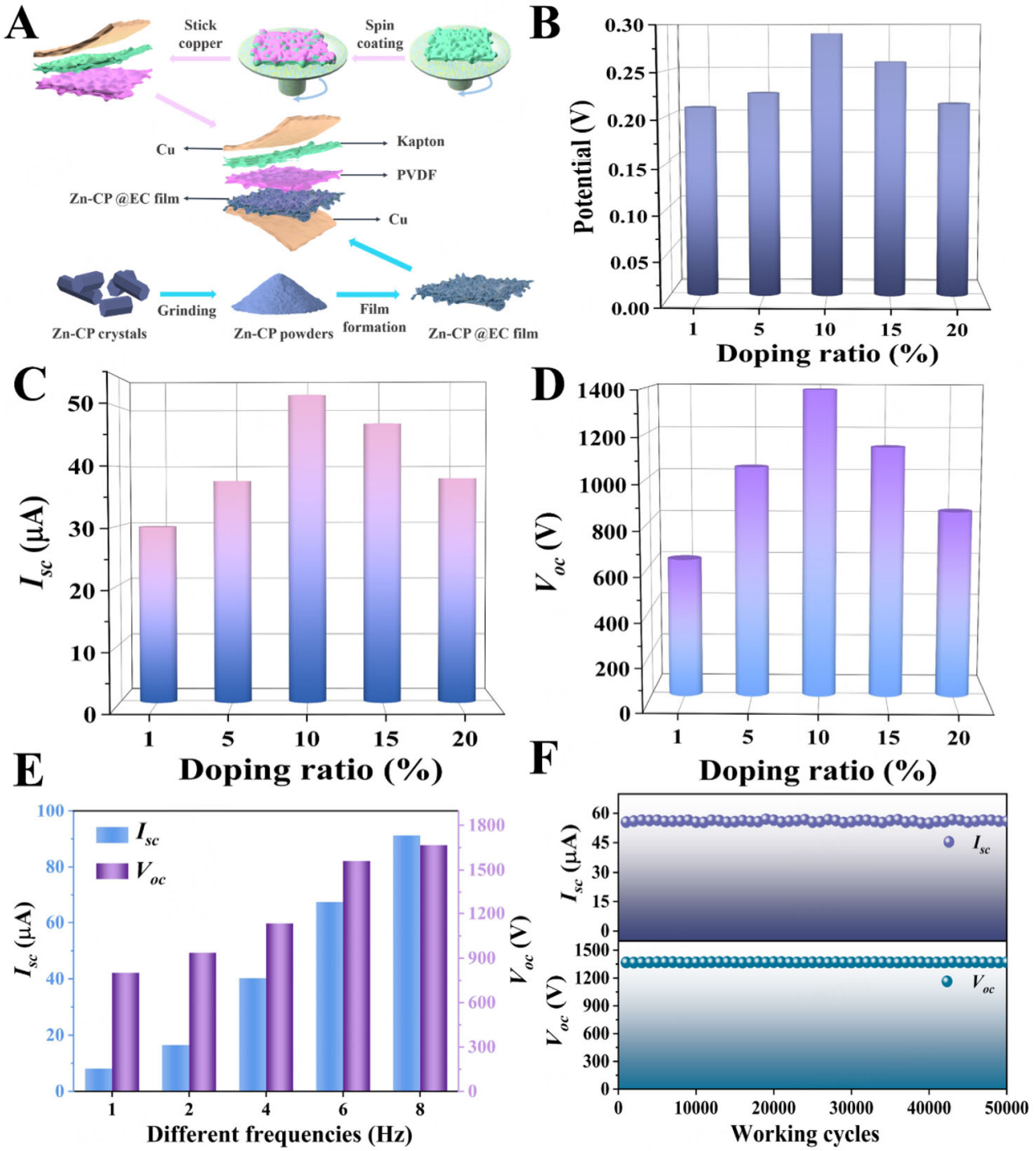


Figure 2. (A) Assembly process of **Zn-CP@EC-based TENG**. (B) KPFM surface potential of **Zn-CP @EC** with different weight ratios, respectively. (C and D) I_{sc} and V_{oc} of the TENGs based on **Zn-CP@EC** with different doping ratios, respectively. (E) I_{sc} and V_{oc} of the TENGs based on **Zn-CP@EC** under different operating frequencies. (F) I_{sc} and V_{oc} of 10% **Zn-CP@EC-based TENG** after working 50,000 cycles.

the electron-donating capacity EC, thereby demonstrating that the 10% **Zn-CP@EC-TENG** output would be best during the continuous and periodic contact between 10% **Zn-CP@EC** composite film and PVDF.

Furthermore, the output of **Zn-CP@EC-TENG** with different proportions was explored at 5 Hz under identical test conditions. As shown in Figure 2C and D, when the **Zn-CP** contents in EC increased from 1% to 10%, the I_{sc} and V_{oc} values of **Zn-CP@EC-TENG** enhanced from 29.8 μA and 626.9 V to 51.9 μA and 1,393.8 V, respectively. This was caused by the enhancement of the tribopositive polarity of the **Zn-CP@EC**

composite films through the interfacial polarization between **Zn-CP** and EC in the composite films[63,64]. Nevertheless, the outputs declined as the **Zn-CP** content rose to 15% or 20%, and the corresponding I_{sc} and V_{oc} peaks for 15% **Zn-CP@EC-TENG** and 20% **Zn-CP@EC-TENG** were 46.7 μA and 1,141.5 V and 37.3 μA and 826.7 V, respectively. This deterioration was attributed to the coacervation of **Zn-CP** within the **Zn-CP@EC** films, which resulted in a poor triboelectric performance and weak mechanical properties[65,66]. These results revealed that the output of **Zn-CP@EC-TENG** was closely related to the **Zn-CP** content of the **Zn-CP@EC** films. The incorporation of low **Zn-CP** concentration improved the **Zn-CP@EC-TENG** output, and the output performance of **Zn-CP@EC-TENG** achieved the largest values when the percentage of **Zn-CP** in **Zn-CP@EC** film was 10%, which was consistent with the results of KPFM surface potentials.

Having successfully built a connection between the **Zn-CP** content in EC and **Zn-CP@EC-TENG** outputs, we next sought to study the environmental suitability and stability by using the optimal 10% **Zn-CP@EC-TENG** device. It could be seen that the outputs (I_{sc} and V_{oc}) of 10% **Zn-CP@EC-TENG** gradually increased as the operating frequency (1-8 Hz) increased, with the largest values at 8 Hz. This observation could be attributed to the reduction in the 10% **Zn-CP@EC-TENG** impedance because of the increased strain [Figure 2E]. The output power density of 10% **Zn-CP@EC-TENG** was examined by employing the formula $P = I^2R$, and the maximum power densities were 4151.2 mW m^{-2} under a load of 30 MΩ [Supplementary Figure 13]. The corresponding outputs of 10% **Zn-CP@EC-TENG** were larger than those of CPs composites or CP-based TENGs [Supplementary Table 3][67-70]. Accordingly, stability and durability tests showed that the 10% **Zn-CP@EC-TENG** output exhibited hardly any significant decrease after 50,000 working cycles [Figure 2F]. In particular, the 10% **Zn-CP@EC-TENG** maintained its original performance even after being retested after two months [Supplementary Figure 14]. Moreover, the 10% **Zn-CP@EC-TENG** worked continuously for 36 h at 5 Hz (equivalent to 648,000 cycles), and the corresponding output performance did not decline significantly [Supplementary Figure 15]. These results confirm that the 10% **Zn-CP@EC-TENG** has excellent cycle performance and stable output, making it suitable for further research.

Subsequently, the corresponding 10% **Zn-CP@EC** composite film and PVDF of the assembled 10% **Zn-CP@EC-TENG** were employed to integrate the zigzag-origami 3D structure devices, which had the flexibility and stretchability to integrate a large number of TENG units for enhancing the output performance. As shown in Figure 3A and Supplementary Figure 16, the zigzag-origami-structured 10% **Zn-CP@EC-TENG** was fabricated from two highly elastic strips that were repeatedly folded to create the compact, elastic device. In **Z-TENGs**, one strip as the tribonegative layer was formed from PVDF, Kapton, Cu, and FEP (fluorinated ethylene propylene) units. The other strip as the tribopositive layer consisted of the 10% **Zn-CP@EC**, Cu, and FEP units. These two flexible equal-length strips could be cyclically folded and staggered to create a zigzag-origami structure with a clear crease pattern, which was beneficial for freeing space to construct a series of multilayered **Z-TENGs**. Furthermore, the **Z-TENGs** displayed good stretching and compression performance during the linear-reciprocating contact-separation process, indicating that only a very small driving force was required to achieve and harvest mechanical energy. As a result, the different contact areas and numbers of origami monomer contact separation **Z-TENGs** composed of two 10% **Zn-CP@EC-TENG** units, named **Z-2**, were designed to explore and optimize output performance by monitoring the hand palm pressing. A series of **Z-2** with different dimensions (1 × 1, 2 × 2, 3 × 3, 4 × 4, and 5 × 5 cm^2, respectively) were designed and fabricated to evaluate the size influence of the triboelectric layer on the output of TENGs [Supplementary Figure 17]. Obviously, the output of **Z-2** is directly proportional to the surface area of the 10% **Zn-CP@EC** triboelectric layer [Figure 3B and C], with the highest output achieved at 25 cm^2. The results indicate that the flexibility and compact design of origami contact-separation **Z-TENGs** make them promising candidates for large-scale assembly by changing the 10% **Zn-CP@EC** triboelectric layer dimensions. After optimizing the effect of the dimensions on the origami **Z-TENGs** to

harvest energy from palm movement, origami **Z-2** with a surface area of 25 cm^2 was integrated in parallel to completely utilize the structural advantage and regulate the output performance. As shown in Supplementary Figure 18, a well-defined 3D platform carrying different numbers of origami **Z-TENG** devices (**Z-2, Z-4,** and **Z-6**) was fabricated in a parallel-circuit configuration, and the corresponding outputs under identical palm-pressure conditions were recorded[71,72]. As shown in Figure 3D and E, the peak I_{sc} of **Z-TENGs** increases with the number of units in parallel, while V_{oc} remains constant, which is due to I_{sc} superposition and unchanged V_{oc} in parallel circuits. The **Z-6** device achieves the maximum output under palm pressure, confirming that array integration of multiple origami **Z-TENGs** is an effective strategy to enhance human motion energy collection performance.

To further simulate and measure the actual application of the **Z-6** device for harvesting environmental energy, a plastic box containing two **Z-6** devices with a copper ball was placed in a water tank to imitate wave motions in the laboratory. As shown in Figure 4A, a motor was used to generate water waves to drive the copper ball back and forth, which leveraged the fluctuation of the waves to realize the contact and separation of the origami **Z-6** device for harnessing wave energy. The corresponding outputs were examined at different water-wave frequencies [Figure 4B and C]. As the operating frequencies increased from 0.4 to 1.2 Hz, the I_{sc} and V_{oc} increased, peaking at 30.9 μA and 372.3 V under 1.2 Hz water waves. The results indicated that as the operating frequency increased, the triboelectric layer contact of **Z-6** in the motion process became more sufficient, resulting in improved output performance. Furthermore, the electronic devices of the thermohygrometer and calculators could be effectively driven by continuously harvesting water-wave energy [Supplementary Videos 1 and 2], demonstrating the outstanding energy supply capacity of self-powered systems without additional storage units [Supplementary Figure 19]. Notably, by collecting water-wave energy, **Z-6** devices quickly lit up a series of LEDs without any energy storage unit [Supplementary Figure 20 and Supplementary Video 3], making them a power supply to produce a successive light source for exploring a self-powered photochemical system.

Subsequently, a self-powered and sustainable photoinduced system was designed by employing origami **Z-6** in an oscillating device to power LEDs, which could serve as a light source for photo-induced reactions. This simple, economical, and eco-friendly self-powered setup, harvests human movement energy, as well as collects wave energy in an oscillating device to convert electrical energy into driving continuous lighting simultaneously. **Z-6** was used in this self-powered photo-induced system to harvest sustainable wave energy and drive LEDs as a light source for performing selective photo-induced reactions. *p*-Tolualdehyde (**2a**) was selected to evaluate the feasibility of the self-powered photo-induced selective oxidation reaction by combining it with **Z-6** as a passive optical device. Preliminary screening experiments demonstrated that oxygen (O_2) exhibited higher selectivity and efficiency than the other oxidants [e.g., air, I_2, H_2O_2, or CF_3SO_2Na, respectively, Supplementary Table 4, entries 1-5]. Based on these results, a range of solvents, atmospheres, and light irradiation were explored [Supplementary Table 4, entries 6-10]. **2a** could be stably converted into the single oxidation product, *p*-toluic acid (**3a**), in the presence of O_2 in H_2O, producing the desired carboxylic acid product **3a** in a comparable yield (98%). Therefore, the most selective self-powered photo-induced oxidation reaction proceeded smoothly under O_2/H_2O/light-irradiation.

The self-powered photo-induced oxidation of **2a** was monitored using ^1H NMR spectroscopy [Supplementary Figure 21]. The peak of δ = 9.96 ppm for singlet hydrogen signal was assigned to the aldehyde group (CHO), which weakened step by step, confirming that self-powered photo-induced oxidation reaction from **2a** to **3a** proceeded stably. Correspondingly, the new singlet signal at δ = 12.80 ppm appeared and strengthened, which was attributable to the carboxyl group. The results demonstrated that product **3a** was generated by prolonging the illumination time, suggesting that the self-powered photo-induced oxidation process was completed.

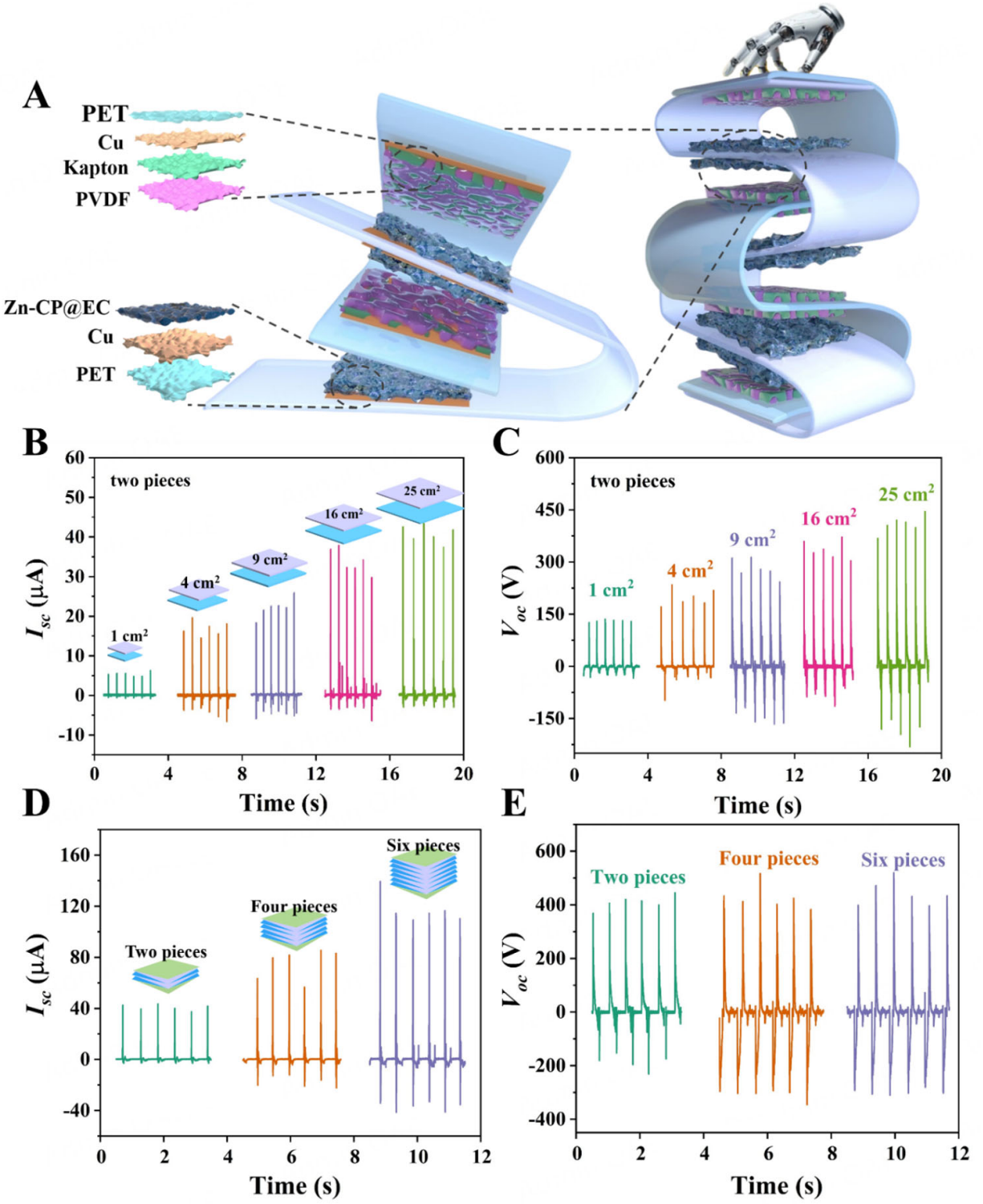


Figure 3. (A) Schematic diagram of **Z-6** device. (B and C) I_{sc} and V_{oc} of 1, 4, 9, 16, and 25 cm² **Z-2**, respectively. (D and E) I_{sc} and V_{oc} of **Z-2**, **Z-4**, **Z-6** measured at 25 cm².

Under standard photocatalytic conditions, various functionalized benzaldehyde-based substrates (**2a-f**) were screened to evaluate their self-powered photo-induced activity [Table 1]. With **Z-6** as the light source, **2a-f** worked well and generated the corresponding carboxylic acid frameworks (**3a-f**) in acceptable-to-good yields. Notably, functional groups such as methyl, methoxy, and hydroxyl as electron-donating groups at the

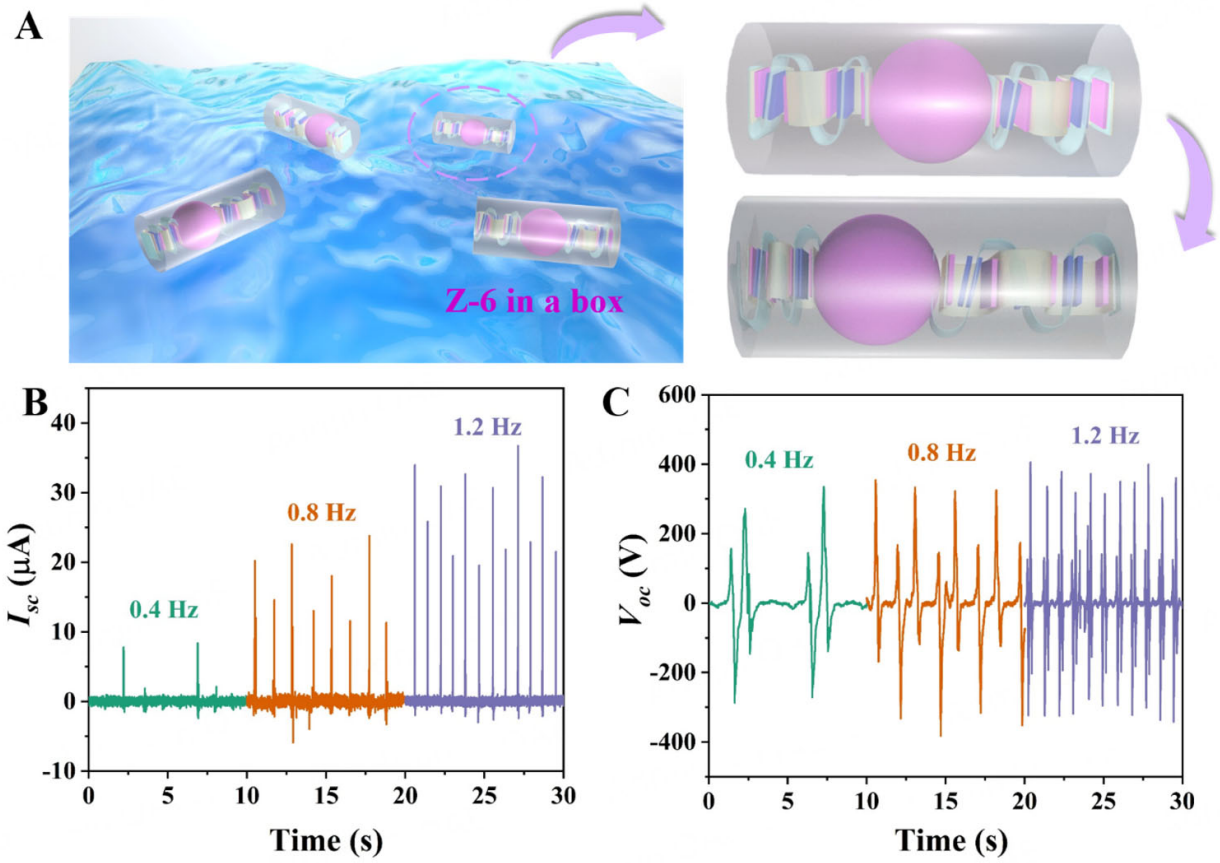
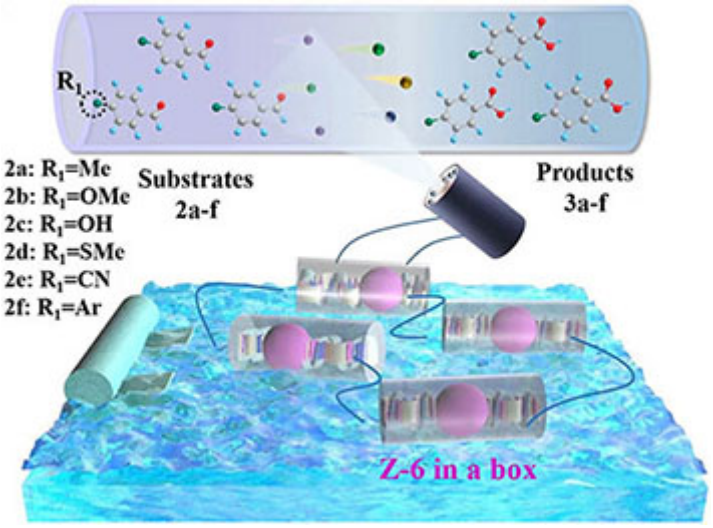


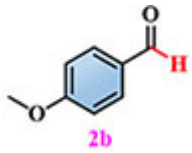
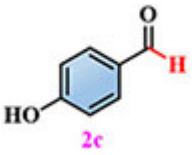
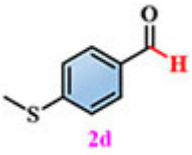
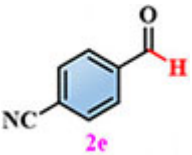
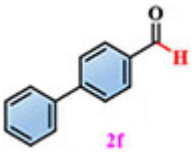
Figure 4. (A) Schematic illustration of water-wave energy harvesting using the **Z-6** device. (B and C) I_{sc} and V_{oc} of water-wave energy harvesting at different frequencies (0.4, 0.8, and 1.2 Hz, respectively).

para-substitution sites on benzaldehyde substrates **2a-c**, were well tolerated under similar reaction conditions and gave the sole benzoic acid products (**3a-c**) in excellent yields [Table 1, entries 1-3]. Importantly, 4-(methylthio)benzaldehyde (**2d**) and 4-cyanobenzaldehyde (**2e**), which bear oxidizable and base-labile groups on their aromatic rings, showed high reactivity and selectivity for desired products **3d** and **3e** [Table 1, entries 4 and 5]. Remarkably, the *p*-phenylbenzaldehyde (**2f**) with a larger bulky size also worked well to produce the active carboxylic acid product (**3f**, 90%) [Table 1, entry 6]. Hence, **Z-6** demonstrated a stable output performance by harvesting water waves to drive LEDs to generate the light source, which indicated good ability to promote the oxidation of aldehydes to carboxylic acids in self-powered photo-induced selective oxidation systems.

Furthermore, a selective self-powered photo-induced oxidation reaction was conducted using 2a as the substrate to explore the relationship between the **Z-6** outputs and conversion efficiencies at 1.2 Hz and different reaction times. As shown in Supplementary Figure 22, the conversion efficiency of **2a** gradually increased from 0% to 19% under light source at 4 h owing to the continuous and stable output of **Z-6**. When the illumination time (8, 12, 16, 20, 24, and 28 h, respectively) was extended, the conversion efficiency of **2a** continued to increase. In contrast, **2a** did not undergo any conversion without **Z-6** to drive the LEDs light source for 28 h. Subsequently, the self-powered photo-induced oxidation process was investigated at different frequencies (0.4, 0.8, and 1.2 Hz, respectively) under similar conditions [Supplementary Figure 23]. It was found that the conversion of **2a** proceeded normally, and the corresponding conversion rates distinctly increased with an increase in **Z-6** output at different frequencies for 28 h. Therefore, these results suggest that changing the light source, reaction times, and working frequencies affected the photo-induced oxidation efficiency but did not affect the oxidation selectivity.

Table 1. Procedure for the light-induced oxidation of aldehydes to carboxylic acids driven by Z-6 devicea



Entry	Substrates 2a-f	Yield of 3a-f (%)[b]
1	 2a	98%
2	 2b	92%
3	 2c	96%
4	 2d	92%
5	 2e	94%
6	 2f	90%

[a]Reaction conditions: 2a-f (0.5 mmol), H_2O (2 mL), O_2, and LEDs (360-365 nm). [b]Isolated yield of the product after 28 h.

To illustrate the mechanism of this oxidation reaction, control measurements were conducted with **2a**. Normally, the results of light irradiation on/off tests revealed that the consecutive light irradiation of LEDs was necessary for the self-powered oxidation of **2a** to **3a** [Supplementary Figure 24]. Furthermore, the inhibition was examined by introducing the radical inhibitor 2, 2, 6, 6-tetramethylpiperidine-1-oxyl (TEMPO), and the corresponding target product **3a** was not produced, which is consistent with the commonly accepted free radical chain process. A plausible mechanism is proposed based on the above results. Originally, the aldehydes were excited and converted to active species **I** under light irradiation. **I** could further generate radical pairs **II** and **III** through hydrogen atom transfer (HAT), which is known to participate in the reaction processes[73,74]. Subsequently, **II** interacted with O_2 to provide peroxy radical **IV**, which could further perform HAT with aldehydes derivatives to generate peracetic acid **V** and radical **II**. The corresponding carboxylic acids were then produced by reacting aldehydes and V through a Baeyer-Villiger rearrangement. Meanwhile, radical **III** reacted with O_2 to give peroxy radical **VI**, which could undergo HAT processes to transform into radical **II** and intermediate peroxide **VII**. **VII** added to the aldehydes to provide intermediate product **VIII**, which underwent intramolecular rearrangement to produce the desired carboxylic acids and aldehydes [Supplementary Scheme 1].

CONCLUSIONS

In summary, we designed and manufactured a flexible origami-structured TENG based on **Zn-CP@EC** composite films, realizing efficient harvesting of low-frequency mechanical energies from human motion and water waves for self-powered selective photo-induced systems. By integrating **Zn-CP** into EC, composite films with tunable triboelectric performance were obtained, among which the 10% **Zn-CP@EC** film delivered optimal and stable electrical output. By optimizing the film dimensions (25 cm^2 as the optimal dimension) and stacking multiple origami units, the six-unit **Z-6** device achieved superior output performance under palm pressure. Its encapsulated configuration efficiently captured wave energy, generating stable electricity to light LEDs as a continuous light source for the photo-induced oxidation of aldehydes to carboxylic acids with high selectivity and efficiency. This study underscores the potential of CP-based composite films as scalable triboelectric materials for multifunctional energy-harvesting applications. Future research will focus on the structural optimization and enhancement of the environmental stability of CPs as well as the expansion of their photochemical applications to advance the practical implementation of CP-based TENGs in green energy conversion and sustainable chemistry.

DECLARATIONS

Authors' contributions

Investigation, methodology, data curation, writing - original draft: Zhao, C.
Supervision, formal analysis, writing - original draft: Zhang, Y. Y.
Validation, visualization: Cui, L.
Project administration, visualization: Wang, D.
Resources, formal analysis: Shao, Z.
Funding acquisition, supervision: Qin, Q.
Resources, writing - review & editing: Hou, H.
Conceptualization, supervision, funding acquisition: Huang, C.

Availability of data and materials

The data presented in this study are available on request from the corresponding author.

AI and AI-assisted tools statement

Not applicable.

Financial support and sponsorship

This work was supported by the National Natural Science Foundation of China (52503283), Program for Innovative Research Team (in Science and Technology) in Universities of Henan Province

(26IRTSTHN041), Program for Science & Technology Innovation Talents in Universities of Henan Province (22HASTIT030), Natural Science Foundation of Henan (252300420270), Program for Science & Technology Innovation Talents in Zhongyuan University of Technology (K2023YXRC02), Training Program for Young Backbone Teachers in Higher Education Institutions in Henan Province (2024GGJS101), Natural Science Foundation of Zhongyuan University of Technology (K2026ZD013), Program for Innovative Research Team of Zhongyuan University of Technology (K2025TD006), Postgraduate Education Reform and Quality Improvement Project of Henan Province (YJS2026AL071), and Postgraduate Education Reform and Quality Improvement Project of Zhongyuan University of Technologye (ALK202511).

Conflicts of interest

All authors declared that there are no conflicts of interest.

Ethical approval and consent to participate

Not applicable.

Consent for publication

Not applicable.

Copyright

© The Author(s) 2026.

Supplementary Materials

Supplementary Materials

REFERENCES

1. Carley, S.; Konisky, D. M. The justice and equity implications of the clean energy transition. *Nat. Energy.* **2020**, *5*, 569-77. DOI
2. Ye, J.; He, C.; Gong, X.; Zhang, H.; Li, X. Blue energy harvesting based on triboelectric nanogenerators (TENG): structural design, performance optimization, and application prospects. *J. Alloys. Compd.* **2025**, *1014*, 178710. DOI
3. Dong, W.; Gao, Z.; Duan, Z.; et al. Sliding-mode cement-based triboelectric nanogenerators in intelligent infrastructure for a new energy harvesting paradigm. *Mater. Today. Energy.* **2025**, *52*, 101943. DOI
4. Wu, X.; Cai, T.; Wu, Q.; et al. Droplet-based triboelectric nanogenerators with needle electrodes for efficient water energy harvesting. *ACS. Appl. Mater. Interfaces.* **2025**, *17*, 13762-72. DOI
5. Yang, Y.; Wang, J.; Qian, W.; Wang, Z. L. Triboelectric nanogenerators as a clean energy scavenging technology. *Mater. Today.* **2025**, *88*, 839-54. DOI
6. Zhang, C.; Hao, Y.; Yang, J.; et al. Magnetic suspension damped hybrid nanogenerator for water wave energy harvesting. *Adv. Energy. Mater.* **2025**, *15*, 2500130. DOI
7. Heo, D.; Hur, J.; Cho, H.; et al. Nano-oil-barrier-based fluttering triboelectric nanogenerator. *Adv. Sci.* **2025**, *12*, e02278. DOI PubMed PMC
8. Davis, S. J.; Lewis, N. S.; Shaner, M.; et al. Net-zero emissions energy systems. *Science* **2018**, *360*, 6396. DOI
9. Sohn, S. H.; Choi, G. J.; On, B. D.; Park, I. K. Synergistic coupling of tribovoltaic and moisture-enabled electricity generation in layered-double hydroxides. *Adv. Energy. Mater.* **2024**, *14*, 2304206. DOI
10. Pan, X.; Yang, X.; Yu, M.; et al. 2D MXenes polar catalysts for multi-renewable energy harvesting applications. *Nat. Commun.* **2023**, *14*, 4183. DOI PubMed PMC
11. Wu, H.; Kang, Y.; Li, K.; et al. Secondary power generation via charge recombination in triboelectric nanogenerators. *ACS. Energy. Lett.* **2024**, *9*, 4516-23. DOI
12. Rani, S.; Khandelwal, G.; Kumar, S.; et al. Flexible self-powered supercapacitors integrated with triboelectric nanogenerators. *Energy. Storage. Mater.* **2025**, *74*, 103977. DOI
13. Gong, S.; Tang, B.; Liu, C.; et al. A synergistically enhanced triboelectric-electromagnetic hybrid generator enabled by multifunctional amorphous alloy for highly efficient self-powered system. *Adv. Mater.* **2025**, *37*, e2412856. DOI
14. Nie, J.; Wang, Z.; Ren, Z.; Li, S.; Chen, X.; Lin, Wang. Z. Power generation from the interaction of a liquid droplet and a liquid membrane. *Nat. Commun.* **2019**, *10*, 2264. DOI
15. Wu, C.; Wang, A. C.; Ding, W.; Guo, H.; Wang, Z. L. Triboelectric nanogenerator: a foundation of the energy for the new era. *Adv. Energy. Mater.* **2018**, *9*, 1802906. DOI

16. Xiang, H.; Peng, L.; Yang, Q.; Wang, Z. L.; Cao, X. Triboelectric nanogenerator for high-entropy energy, self-powered sensors, and popular education. *Sci. Adv.* **2024**, *10*, eads2291. DOI
17. Rui, P.; Zhang, W.; Wang, P. Super-durable and highly efficient electrostatic induced nanogenerator circulation network initially charged by a triboelectric nanogenerator for harvesting environmental energy. *ACS. Nano.* **2021**, *15*, 6949-60. DOI
18. Zhang, Q.; Li, Y.; Cai, H.; et al. A single-droplet electricity generator achieves an ultrahigh output over 100 V without pre-charging. *Adv. Mater.* **2021**, *33*, e2105761. DOI
19. Zhang, C.; Hao, Y.; Lu, X.; et al. Advances in TENGs for marine energy harvesting and in situ electrochemistry. *Nanomicro. Lett.* **2025**, *17*, 124. DOI PubMed PMC
20. Chi, M.; Cai, C.; Liu, Y.; et al. Aramid triboelectric materials: opportunities for self-powered wearable personal protective electronics. *Adv. Funct. Mater.* **2024**, *34*, 2411020. DOI
21. Wang, T.; Shen, Y.; Chen, L.; et al. Large-scale production of the 3D warp knitted terry fabric triboelectric nanogenerators for motion monitoring and energy harvesting. *Nano. Energy.* **2023**, *109*, 108309. DOI
22. Hou, K.; Dai, X.; Zhao, S.; Huang, L.; Li, C. A damage-tolerant, self-healing and multifunctional triboelectric nanogenerator. *Nano. Energy.* **2023**, *116*, 108739. DOI
23. Kovalska, E.; Lam, H. T.; Saadi, Z.; et al. Textile beeswax triboelectric nanogenerator as self-powered sound detectors and mechano-acoustic energy harvesters. *Nano. Energy.* **2024**, *120*, 109109. DOI
24. Zhang, F.; Zheng, L.; Li, H.; et al. Multifunctional triboelectric nanogenerator for wind energy harvesting and mist catching. *Chem. Eng. J.* **2024**, *488*, 150875. DOI
25. Yang, R. A multifunctional triboelectric nanogenerator based on PDMS/MXene for bio-mechanical energy harvesting and volleyball training monitoring. *Heliyon* **2024**, *10*, e32361. DOI
26. Yun, J.; Kim, D. Self-powered triboelectricity-driven multiple-input-single-output occupancy detection system using a triboelectric nanogenerator for energy management. *Polymers* **2024**, *17*, 34. DOI
27. Han, J.; Dai, X.; Huang, L.; Hao, J. Optimizing electrical output performance of triboelectric nanogenerators by micro-/nano-morphology design and fabrication. *Int. J. Extrem. Manuf.* **2025**, *7*, 032008. DOI
28. Liu, D.; Yang, P.; Gao, Y.; et al. A dual-mode triboelectric nanogenerator for efficiently harvesting droplet energy. *Small* **2024**, *20*, e2400698. DOI
29. Lou, Y.; Li, M.; Yu, A.; Zhai, J.; Wang, Z. L. From wave energy to electricity: functional design and performance analysis of triboelectric nanogenerators. *Nanomicro. Lett.* **2025**, *17*, 298. DOI PubMed PMC
30. Kim, W. G.; Kim, D. W.; Tcho, I. W.; Kim, J. K.; Kim, M. S.; Choi, Y. K. Triboelectric nanogenerator: structure, mechanism, and applications. *ACS. Nano.* **2021**, *15*, 258-87. DOI
31. Liang, X.; Jiang, T.; Liu, G.; Feng, Y.; Zhang, C.; Wang, Z. L. Spherical triboelectric nanogenerator integrated with power management module for harvesting multidirectional water wave energy. *Energy. Environ. Sci.* **2020**, *13*, 277-85. DOI
32. Alghamdi, M. S.; Morgan, J. J.; Walsh, K.; et al. Triboelectric nanogenerator based on cellulose nanocrystals and graphene for energy harvesting from piano playing motion. *Nano. Energy.* **2025**, *138*, 110816. DOI
33. Jiao, Y.; Lin, Z.; Guo, X.; et al. Compositional engineering of hybrid organic-inorganic lead-halide perovskite and PVDF-graphene for high-performance triboelectric nanogenerators. *ACS. Appl. Mater. Interfaces.* **2024**, *16*, 3532-41. DOI
34. Fan, J.; Yang, R.; Du, Y.; et al. A triboelectric nanogenerator based on MXene/TPU composite films with excellent stretchability for self-powered flexible sensing. *Nano. Energy.* **2024**, *129*, 109999. DOI
35. Tan, X.; Wang, S.; You, Z.; Zheng, J.; Liu, Y. High performance porous triboelectric nanogenerator based on silk fibroin@MXene composite aerogel and PDMS sponge. *ACS. Materials. Lett.* **2023**, *5*, 1929-37. DOI
36. Rani, G. M.; Kim, H.; Pammi, S. V. N.; Umapathi, R.; Huh, Y. S. Next-generation flexible and wearable triboelectric nanogenerator based on PVDF-HFP@GCN composite for mechanical energy scavenging and sleep pattern detection. *Adv. Funct. Mater.* **2025**, *36*, e19594. DOI
37. Gajula, P.; Yoon, J. U.; Woo, I.; Bae, J. W. Harnessing mechanical energy for green hydrogen: pioneering high-performance triboelectric nanogenerators. *Adv. Funct. Mater.* **2025**, *35*, 2501074. DOI
38. Shao, Z.; Chen, J.; Xie, Q.; Mi, L. Functional metal/covalent organic framework materials for triboelectric nanogenerator. *Coord. Chem. Rev.* **2023**, *486*, 215118. DOI
39. Wen, R.; Feng, R.; Zhao, B.; Song, J.; Fan, L.; Zhai, J. Controllable design of high-efficiency triboelectric materials by functionalized metal - organic frameworks with a large electron-withdrawing functional group. *Nano. Res.* **2022**, *15*, 9386-91. DOI
40. Collins, S. P.; Daff, T. D.; Piotrkowski, S. S.; Woo, T. K. Materials design by evolutionary optimization of functional groups in metal-organic frameworks. *Sci. Adv.* **2016**, *2*, e1600954. DOI PubMed PMC
41. Lin, C.; Sun, L.; Meng, X.; et al. Covalent organic frameworks with tailored functionalities for modulating surface potentials in triboelectric nanogenerators. *Angew. Chem. Int. Ed.* **2022**, *61*, e202211601. DOI

42. Yu, X.; Ge, J.; Wang, Z.; et al. High-performance triboelectric nanogenerator with synchronization mechanism by charge handling. *Energy. Convers. Manag.* **2022**, *263*, 115655. DOI
43. Zhang, Y.; Zhang, Z.; Peng, W.; et al. Bionic wood-inspired structure enables aerogel film triboelectric material with humidity adaptation. *Chem. Eng. J.* **2024**, *497*, 154906. DOI
44. Fu, C.; Han, X.; Zhang, Y.; Hu, J.; Du, J.; Wang, H. Synergistic functionality of metal-organic framework-cellulose composites structures for advanced high-performance energy materials. *Chem. Eng. J.* **2025**, *503*, 158384. DOI
45. Pander, M.; Gil-San-Millan, R.; Delgado, P.; et al. MOF/polymer hybrids through in situ free radical polymerization in metal-organic frameworks. *Mater. Horiz.* **2023**, *10*, 1301-8. DOI PubMed PMC
46. Su, X.; Cheng, L.; Yan, X.; et al. In situ construction of amide-functionalized 2D conjugated metal-organic frameworks with multiple active sites for high-performance potassium-ion batteries. *J. Am. Chem. Soc.* **2025**, *147*, 18338-48. DOI
47. Esposito, M. R.; Newar, R.; Kim, M.; Cohen, S. M. Incorporation of low-valent metal ions in metal-organic frameworks and coordination polymers. *Coord. Chem. Rev.* **2025**, *531*, 216491. DOI
48. Ma, R.; Hou, Y.; Zhang, W.; Pan, Y.; Huo, S.; Shi, C. MOF-based nanocomposites in polymer matrix: progress and prospects. *Adv. Compos. Hybrid. Mater.* **2025**, *8*, 351. DOI
49. Salahshoori, I.; Golriz, M.; Namayandeh, Jorabchi. M.; Moghari, S.; Khonakdar, H. A. Recent progress in MOF-based biopolymer composites for wastewater detoxification. *Coord. Chem. Rev.* **2025**, *543*, 216919. DOI
50. Rana SM, Faruk O, Selim Reza M, Robiul Islam M, Kim H, Yeong Park J. All porous Ecoflex and SEBS-based stretchable high-performance triboelectric nanogenerator for self-powered human activity monitoring. *Chem. Eng. J.* **2024**, *488*, 151050. DOI
51. Wan, H.; Fang, Y.; Hu, M.; et al. Interpretable machine-learning and big data mining to predict the CO_2 separation in polymer-MOF mixed matrix membranes. *Adv. Sci.* **2025**, *12*, e2405905. DOI PubMed PMC
52. Feng, H.; Li, H.; Xu, J.; et al. Triboelectric nanogenerator based on direct image lithography and surface fluorination for biomechanical energy harvesting and self-powered sterilization. *Nano. Energy.* **2022**, *98*, 107279. DOI
53. Wang, F.; Zhang, Y.; Li, S.; et al. Integration of cobalt coordination polymer-based triboelectric nanogenerators as sustainable power sources for self-driven selective photocatalytic reactions. *Chem. Eng. J.* **2025**, *503*, 158194. DOI
54. Wang, X.; Ye, C.; Chen, P.; et al. Achieving high power density and durability of multilayered swing-structured triboelectric nanogenerator toward marine environmental protection. *Adv. Funct. Mater.* **2023**, *34*, 2311196. DOI
55. Higoshi, H.; Naritomi, D.; Kamiyauchi, S.; et al. Self-folded corrugated origami sensor based on triboelectric nanogenerator for a smart cushioning device. *Adv. Mater. Technol.* **2025**, *10*, 2500032. DOI
56. Wu, G.; Xu, M.; Lei, M.; et al. Full-fiber triboelectric nanogenerators with knitted origami structures for high impact resistance intelligent protection fabric. *Mater. Horiz.* **2025**, *12*, 1246-54. DOI
57. Hong, H.; Yang, X.; Cui, H.; et al. Self-powered seesaw structured spherical buoys based on a hybrid triboelectric-electromagnetic nanogenerator for sea surface wireless positioning. *Energy. Environ. Sci.* **2022**, *15*, 621-32. DOI
58. Shan, C.; He, W.; Wu, H.; et al. Dual mode TENG with self-voltage multiplying circuit for blue energy harvesting and water wave monitoring. *Adv. Funct. Mater.* **2023**, *33*, 2305768. DOI
59. Zheng, Z.; Xia, J.; Wang, B.; Guo, Y. Hierarchically designed nanocomposites for triboelectric nanogenerator toward biomechanical energy harvester and smart home system. *Nano. Energy.* **2022**, *95*, 107047. DOI
60. Huang, C.; Zhu, K.; Zhang, Y.; et al. Surfactant-assisted assembly of nanoscale zinc coordination compounds to enhance tandem conversion reactions in water. *Dalton. Trans.* **2019**, *48*, 16008-16. DOI
61. Xiang, L.; Tang, C.; Xu, Z.; Xu, F.; Li, C.; Mai, Y. Functional porous cubosomes: synthesis and applications in energy storage and conversion. *Acc. Mater. Res.* **2025**, *6*, 939-51. DOI
62. Heine, T.; Dinca, M.; Zhu, G. Physical phenomena in porous frameworks. *Acc. Chem. Res.* **2025**, *58*, 327-9. DOI PubMed
63. Si, H.; Lee, D.; Park, D.; et al. Size effects of polydopamine-coated $BaTiO_3$ nanoparticles on the piezoelectric performance of P(VDF-TrFE)/$BaTiO_3$ composite. *J. Materiomics.* **2024**, *10*, 857-69. DOI
64. Luo, J.; Wang, Y. Effect of hierarchical layer structure design on the sensing performances of $NaNbO_3$/P(VDF-TrFE) piezoelectric composite films. *J. Alloys. Compd.* **2025**, *1017*, 179071. DOI
65. Lee, C. H.; Min, K. A.; Park, H. B.; Hong, Y. T.; Jung, B. O.; Lee, Y. M. Sulfonated poly(arylene ether sulfone)-silica nanocomposite membrane for direct methanol fuel cell (DMFC). *J. Membr. Sci.* **2007**, *303*, 258-66. DOI
66. Shalu, S.; Kar, P.; Krupka, J.; Dasgupta, Ghosh. B. Synthesis, characterization, thermal, dynamic mechanical, and dielectric studies of $Ba_{0.7}Sr_{0.3}TiO_3$/polystyrene composites. *Polym. Compos.* **2018**, *39*, 1714-24. DOI
67. Bochu, L.; Babu, A.; Potu, S.; Khanapuram, U. K.; Rajaboina, R. K.; Kodali, P. Enhancing triboelectric nanogenerator performance with metal-organic framework composite nanofibers: applications in public transit monitoring, staircase alerts, and security. *ACS. Appl. Polym. Mater.* **2025**, *7*, 4132-41. DOI

68. Graham, S. A.; Kurakula, A.; Kavarthapu, V. S.; et al. Metal-organic framework embedded electrospun fibrous membranes-based hybrid nanogenerators with hierarchical modified polyamide films for mechanical energy harvesting and IoT applications. *Adv. Funct. Mater.* **2025**, *36*, e07125. DOI
69. Salauddin, M.; Rana, S. S.; Sharifuzzaman, M.; et al. Laser-carbonized MXene/ZiF-67 nanocomposite as an intermediate layer for boosting the output performance of fabric-based triboelectric nanogenerator. *Nano. Energy.* **2022**, *100*, 107462. DOI
70. Xiong, J.; Cui, P.; Chen, X.; et al. Skin-touch-actuated textile-based triboelectric nanogenerator with black phosphorus for durable biomechanical energy harvesting. *Nat. Commun.* **2018**, *9*, 4280. DOI PubMed PMC
71. Wu, Y.; Zhang, D.; Zhang, Y.; et al. Water wave energy-harvesting accordion structure triboelectric nanogenerators for self-driven corrosion protection. *Nano. Energy.* **2025**, *142*, 111207. DOI
72. Xu, L.; Pang, Y.; Zhang, C.; et al. Integrated triboelectric nanogenerator array based on air-driven membrane structures for water wave energy harvesting. *Nano. Energy.* **2017**, *31*, 351-8. DOI
73. Xu, J.; Yue, X.; He, L.; et al. Photoinduced protocol for aerobic oxidation of aldehydes to carboxylic acids under mild conditions. *ACS. Sustain. Chem. Eng.* **2022**, *10*, 14119-25. DOI
74. Shi, H.; Li, J.; Wang, T.; Rudolph, M.; Hashmi, A. S. K. Catalyst- and additive-free sunlight-induced autoxidation of aldehydes to carboxylic acids. *Green. Chem.* **2022**, *24*, 5835-41. DOI

Disclaimer/Publisher's Note: All statements, opinions, and data contained in this publication are solely those of the individual author(s) and contributor(s) and do not necessarily reflect those of OAE and/or the editor(s). OAE and/or the editor(s) disclaim any responsibility for harm to persons or property resulting from the use of any ideas, methods, instructions, or products mentioned in the content.


© The Author(s) 2026. Open Access This article is licensed under a Creative Commons Attribution 4.0 International License (https://creativecommons.org/licenses/by/4.0/), which permits unrestricted use, sharing, adaptation, distribution and reproduction in any medium or format, for any purpose, even commercially, as long as you give appropriate credit to the original author(s) and the source, provide a link to the Creative Commons license, and indicate if changes were made.